Research Article

ADVANCED PHOTONICS

Giant photoinduced reflectivity modulation of nonlocal resonances in silicon metasurfaces

Andrea Tognazzi,[a,b] Paolo Franceschini,[b,c,*] Olga Sergaeva,[c,d] Luca Carletti,[b,c] Ivano Alessandri,[b,c] Giovanni Finco,[e] Osamu Takayama,[f] Radu Malureanu,[f] Andrei V. Lavrinenko,[f] Alfonso C. Cino,[a] Domenico de Ceglia,[b,c] and Costantino De Angelis[b,c]

[a]University of Palermo, Department of Engineering, Palermo, Italy
[b]National Institute of Optics-National Research Council, Brescia, Italy
[c]University of Brescia, Department of Information Engineering, Brescia, Italy
[d]ITMO University, School of Physics and Engineering, Saint-Petersburg, Russia
[e]ETH Zurich, Institute for Quantum Electronics, Department of Physics, Optical Nanomaterial Group, Zurich, Switzerland
[f]Technical University of Denmark, Department of Electrical and Photonics Engineering, Kongens Lyngby, Denmark

Abstract. Metasurfaces offer a unique playground to tailor the electromagnetic field at subwavelength scale to control polarization, wavefront, and nonlinear processes. Tunability of the optical response of these structures is challenging due to the nanoscale size of their constitutive elements. A long-sought solution to achieve tunability at the nanoscale is all-optical modulation by exploiting the ultrafast nonlinear response of materials. However, the nonlinear response of materials is inherently very weak, and, therefore, requires optical excitations with large values of fluence. We show that by properly tuning the equilibrium optical response of a nonlocal metasurface, it is possible to achieve sizable variation of the photoinduced out-of-equilibrium optical response on the picosecond timescale employing fluences smaller than 250 μJ/cm^2, which is 1 order of magnitude lower than previous studies with comparable reflectivity variations in silicon platforms. Our results pave the way to fast devices with large modulation amplitude.

Keywords: nonlocal metasurface; nanophotonics; ultrafast modulation; Fano resonance.

Received Sep. 6, 2023; revised manuscript received Oct. 10, 2023; accepted for publication Nov. 1, 2023; published online Dec. 9, 2023.

[DOI: 10.1117/1.AP.5.6.066006]

1 Introduction

In the last few decades, the advent of nanofabrication technologies has boosted the interest in optical devices working in the visible and near-infrared (NIR) region. Metasurfaces are two-dimensional arrangements of nanostructures (or subwavelength elements), called meta-atoms, which allow one to tailor the electromagnetic field at the nanoscale, thus surpassing the capabilities of bulk materials.[1,2] The possibility of introducing abrupt changes in phase and amplitude is of paramount importance to focusing,[3,4] polarization control,[5] nonlinear frequency conversion,[6] and wavefront manipulation.[7]

Providing methods to dynamically control a nanoscale device is mandatory to produce flexible and effective tools to manipulate light. The compact nature of such devices allows one to reach faster modulation speed employing approaches that are traditionally slower tuning mechanisms, such as heating and mechanical strain.[8–11] Liquid crystals have also been employed to rapidly change the optical response of metasurfaces to achieve multifunctional behavior[12] and phase tuning.[13] Phase-change materials have been proposed as suitable platforms to obtain large all-optical modulation featuring vast versatility of the activation mechanisms.[14–18] So far, optical excitation provides the fastest modulation source allowing ultrafast dynamic control of nanophotonic devices.[19–21] Originally, the strong optical nonlinearities in plasmonic meta-atoms were first investigated as a route toward ultrafast nanophotonics.[22] Subsequently, their ohmic losses at optical frequencies and the poor compatibility with large-scale CMOS integration opened the way for the advent of all-dielectric structures, which have already been

*Address all correspondence to Paolo Franceschini, paolo.franceschini@unibs.it

demonstrated to achieve ultrafast control of polarization, amplitude, and wavefront.[21,23–26] In all-optically modulated devices, the ultrafast two-photon absorption (TPA) and free carrier (FC) generation dynamics come along with thermal effects related to lattice heating, which take place at the nanosecond timescale.[27] Recently, it was demonstrated that by properly engineering the metasurface, it is possible to achieve a full recovery of the optical response on the picosecond timescale.[23,25] However, the entity of such modulation is often small, usually below a few percent, and requires large fluences, i.e., energy densities.[23,25,28] Therefore, the detection of such tiny variations is laborious and requires bulky and expensive experimental setups, annihilating the miniaturization advantages of optical devices.

Here we design a high-contrast nonlocal metasurface (NLM) based on silicon (Si) meta-atoms lying on silica (SiO_2) pedestals that exhibits a guided mode resonance (GMR) in the NIR spectral region, and we show giant all-optical relative reflectance variation (up to 60%) on the picosecond timescale. We use time- and wavelength-resolved spectroscopy to investigate the out-of-equilibrium temporal dynamics of the nonlocal NIR resonance following FC injection. In particular, we perform pump–probe experiments to address the carrier and lattice dynamical processes and their role on the time evolution of the spectral signature of the nonlocal resonance. We show a transient photoinduced modulation of the optical properties of NLM (i.e., resonant gratings), which is 1 order of magnitude larger than the unpatterned platform (under the same excitation conditions). The analysis of the experimental data, combining a coupled rate equations model (CREM) and rigorous coupled-wave analysis (RCWA), allows one to disentangle the role of the photonic structure and the modulation of the optical properties (due to FCs and lattice heating effects) and reveals a decrease of the carrier recombination time with respect to bulk material. Our results have direct impact in the design of next-generation ultrafast all-optical modulators and switches with reduced energy consumption, since we demonstrate an increase of 1 order of magnitude in the relative reflectance variation, with fluences below 250 $\mu J/cm^2$, with respect to unstructured silicon.

2 Results and Discussion

We employ an NLM, which we previously demonstrated[29] to feature sharp spectral resonance with large amplitude in the third operating window of optical communications, to unveil the pivotal role of the photonic structure to achieve large amplitude modulation with smaller fluence compared to bulk materials. The high-index-contrast NLM under analysis, shown in Fig. 1(a), is based on a Si grating (width $w = 393$ nm, height $d = 500$ nm, and periodicity $P = 820$ nm), supported by silica (SiO_2) pedestals (height $h_p = 160$ nm and width $w_p = 73$ nm) to achieve high-index contrast with the environment, i.e., between air and the lower-lying SiO_2 layer. We engrave the Si grating within a silicon-on-insulator substrate combining deep ultraviolet (DUV) lithography and reactive ion etching. The total thickness of the SiO_2 layer is $h = 1160$ nm (see Appendix A).

The equilibrium optical properties of the NLM are shown in Fig. 1(b). Here we display the experimental (markers) reflectance spectrum at equilibrium (R_{eq}) as a function of the wavelength (λ) measured by a broadband NIR probe light linearly polarized along the direction parallel to the grating bars, x axis in the present work [see Fig. 1(a)], which corresponds to a transverse electric (TE) polarization (see Appendix B).

The sharp spectral feature at around 1380 nm, arising on top of a background due to Fabry–Perot modes, is ascribed to a GMR (quality factor $Q_F \sim 170$; see Fig. S3 in the Supplementary Material), which is mediated by a leaky mode propagating along the grating periodicity direction (y axis).[29] The leaky nature of the GMR can be deduced by looking at the spatial distribution of the mode in Fig. 1(b) (see inset). To model the NLM equilibrium properties, we calculate the reflectance through RCWA as the normalized intensity of the reflected radiation along the zeroth order (see Appendix C for more details). The resulting calculated reflectance spectrum $R^{eq}_{RCWA}(\lambda)$ [red solid line in Fig. 1(b)] shows a fairly good agreement with the experimental data, reproducing the line shape of the GMR, manifesting as a Fano resonance. This originates from the coupling of the discrete spectrum of the leaky GMR to the continuum of modes of the incident light.[30] Discrepancy in the

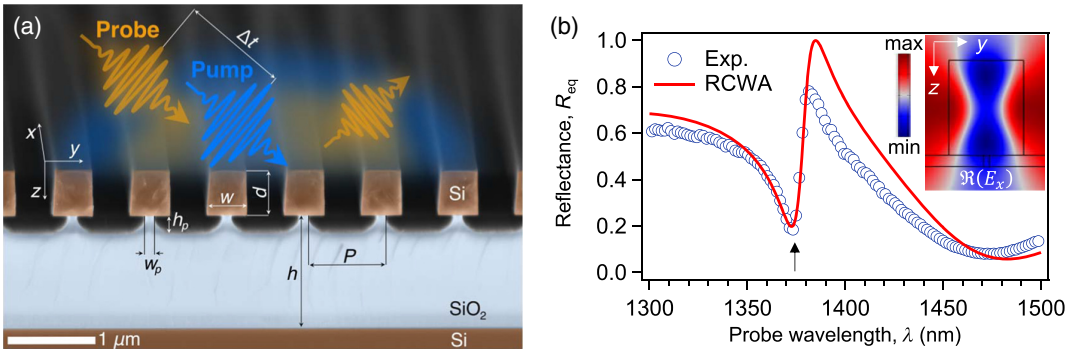

Fig. 1 (a) Sketch of the experiment working principle: a pump pulse (blue) excites the sample and changes the optical properties of silicon (brown). A delayed low-intensity probe pulse (yellow) monitors the reflectivity changes. The image is a false color scanning electron micrograph of the NLM. Dimensions: $w = 393$ nm, $d = 500$ nm, $P = 820$ nm, $w_p = 73$ nm, $h_p = 160$ nm, and $h = 1160$ nm. (b) Experimental (circles) and calculated (RCWA, red solid line) reflectance spectra (R_{eq}) at equilibrium. The inset shows the TE mode spatial distribution in the yz plane (orthogonal to the grating) at 1375-nm wavelength (black arrow).

spectra may originate from the dispersion of the geometrical parameters (due to fabrication tolerances) or minimum differences of the pedestal profile within the sample area detected by the probe beam (see Ref. [29] for more details). Nevertheless, the model reveals the collective (i.e., nonlocal) nature of the resonance and the eigenmode analysis allows one to correctly locate its spectral position at $\lambda_\Gamma^{\mathrm{eq}} \simeq 1375$ nm.

We perform a time- and wavelength-resolved pump–probe spectroscopy experiment to monitor the time evolution of the GMR following photoexcitation. In general, in bulk Si, the carrier relaxation dynamics evolves according to the following well-established picture.[31,32] Upon photoexcitation by a pump pulse with photon energy ($E_p = 2\pi\hbar c/\lambda_p$, where λ_p is the pump wavelength), which can be larger (or smaller) than the bandgap E_g, an FC density N is photogenerated within the bands (electrons in the conduction band and holes in the valence band) by linear (or nonlinear) absorption processes. The initial coherently excited carrier states undergo dephasing processes via carrier–carrier and carrier–phonon scattering mechanisms. This coherent regime (~30 fs for Si[32]) is followed by a nonthermal regime (on a timescale of 100 to 300 fs[33,34]) during which a carrier temperature is established via collisions. This allows one to describe the carrier population in terms of Fermi–Dirac distribution, with the carrier and lattice temperature depending on E_p. Finally, as time evolves, hot carriers cool down via energy exchange with the lattice (accompanied by optical phonon scattering).

In our experiment, as depicted in Fig. 1(a), a short-pump laser pulse centered at $\lambda_p = 410$ nm (i.e., in the absorption region of Si) first induces a variation of the optical properties of the NLM via FC generation. Then a broadband probe laser pulse, tuned in the GMR spectral region (1340 to 1400 nm range), impinges at delay time Δt after the pump, thus monitoring the out-of-equilibrium state of the system (see Appendix D for more details). The probe beam spot size [beam waist radius $w_0^{(\mathrm{probe})} = (75 \pm 5)\ \mu$m], smaller than the pump one [$w_0^{(\mathrm{pump})} = (120 \pm 10)\ \mu$m], has been chosen to ensure the illumination of a minimum number of periods (N_P) to avoid the beam size effects (based on Ref. [35], for the NLM under analysis $N_P = Q_F/\pi \sim 54$).

We measure the relative reflectance variation ($\Delta R/R$) defined as the difference ($\Delta R = R_{\mathrm{out}} - R_{\mathrm{eq}}$) between the reflected light with and without the pump (R_{out} and R_{eq}, respectively) normalized to the reflected light spectrum without the pump.

Measured $\Delta R/R$ spectra at various delay times (Δt), in the timescale below 100 ps, are reported in Fig. 2(a) (see also Fig. S2 in the Supplementary Material for additional details on the the corresponding R_{out} spectra). Here we use an incident pump fluence $F_{\mathrm{inc}} = (180 \pm 30)\ \mu\mathrm{J/cm}^2$ to ensure that we photoexcite the NLM in the linear regime. We underline that this value is much lower than in other studies with comparable, or even smaller, variations of the reflectivity in Si-based platforms.[23,25,28,36] The $\Delta R/R(\lambda, \Delta t)$ signal is mainly characterized by two long-living components: a negative dip at $\lambda \simeq 1370$ nm and a positive peak at $\lambda \simeq 1375$ nm; these correspond to the spectral regions below and above the minimum of the Fano resonance [see Fig. 1(b)]. The additional change of the sign in the out-of-equilibrium spectra at $\lambda > 1380$ nm corresponds to the spectral region above the Fano resonance peak. As far as the amplitude of the out-of-equilibrium signal is concerned, we observe a giant relative reflectance variation of 50% ($R_{\mathrm{eq}} = 0.18$ and $R_{\mathrm{out}} = 0.27$) at $\Delta t = 3$ ps for $\lambda \simeq 1373$ nm.

In order to gain further insights into the interplay between the nonequilibrium photoinjected FCs and the geometry-controlled GMR, we simulate the out-of-equilibrium response of NLM with a theoretical approach combining the CREM, accounting for FC concentration and lattice temperature dynamics, and RCWA, describing light–matter interaction in the NLM. The differential spectra shown in Fig. 2(b) are calculated as $\Delta R/R(\lambda, \Delta t) = R^{\mathrm{out}}_{\mathrm{RCWA}}(\lambda, \Delta t)/R^{\mathrm{eq}}_{\mathrm{RCWA}}(\lambda) - 1$. The time-dependent out-of-equilibrium reflectivity spectrum $R^{\mathrm{out}}_{\mathrm{RCWA}}(\lambda, \Delta t)$ is obtained from a perturbed Si dielectric function ($\varepsilon_{\mathrm{out}} = \varepsilon_{\mathrm{Si}} + \Delta\varepsilon$, with $\varepsilon_{\mathrm{Si}}$ being the equilibrium Si dielectric function and $\Delta\varepsilon$ the photoinduced variation) to account for the effect of photogenerated carriers. In particular, we assume that the total variation $\Delta\varepsilon$ includes both linear and nonlinear contributions, where the former is ascribed to mechanisms involving the FCs and the lattice (L), and the latter is related to the TPA; therefore, $\Delta\varepsilon = \Delta\varepsilon_{\mathrm{FC}} + \Delta\varepsilon_L + \Delta\varepsilon_{\mathrm{TPA}}$. For the sake of completeness, we mention that, in addition to the previous effects, also state filling (SF) and bandgap renormalization (BGR) mechanisms[37,38] may represent a linear-response contribution to $\Delta\varepsilon$. However, taking into account that the considered probing region is located in a spectrum far from the bandgap, i.e., the spectral region where SF and BGR mainly dominate, we neglect their contribution in the calculation of the $\Delta R/R$ spectra.

Regarding FCs, their contribution is mainly described in terms of the Drude model; therefore, we assume the change of the dielectric constant of the material due to FC generation in the form[37,39]

$$\Delta\varepsilon_{\mathrm{FC}}(\lambda, \Delta t) = -N(\Delta t)e^2 \cdot \left(1 - i\frac{\lambda}{2\pi c\tau_d}\right) \cdot \left(\frac{4\pi^2 c^2 m_{\mathrm{eff}}\varepsilon_0}{\lambda^2} + \frac{1}{\tau_d^2}\right)^{-1}, \tag{1}$$

where e is the electron charge, c is the velocity of light in vacuum, τ_d is the Drude damping time, m_{eff} is the effective mass of electrons and holes, and ε_0 is the vacuum permittivity. As mentioned, the relaxation of FCs within the bands, occurring via a first-order trap-assisted process (with characteristic time τ_{rFC}) or via second-order bimolecular recombination (at rate γ), is accompanied by lattice heating; its contribution to the optical modulation occurs via the thermo-optic effect, which has been modeled as follows:[32,40]

$$\Delta\varepsilon_L(\lambda, \Delta t) = 2 \cdot \sqrt{\varepsilon_{\mathrm{Si}}(\lambda)} \cdot \eta_1(\lambda) \cdot T(\Delta t), \tag{2}$$

where T is the lattice temperature (recovering the equilibrium value with a characteristic timescale τ_{rL}) and η_1 is the Si thermo-optic coefficient. Third, the nonlinear absorption (due to TPA) has been implemented as follows:[25]

$$\Delta\varepsilon_{\mathrm{TPA}}(\Delta t) = \Re\left[\sqrt{\varepsilon_{\mathrm{Si}}(\lambda_p)}\right] \cdot \frac{\beta_{\mathrm{TPA}} I(\Delta t)\lambda_p}{2\pi}, \tag{3}$$

where β_{TPA} is the Si nonlinear absorption coefficient and I the impinging pump intensity (see Appendix C). The temporal dependence in Eqs. (1)–(3) is a consequence of the temporal dynamics of the three quantities $N(\Delta t)$, $T(\Delta t)$, and $I(\Delta t)$, described by the two-coupled rate equations in Eq. (4) (see Appendix C for more details).

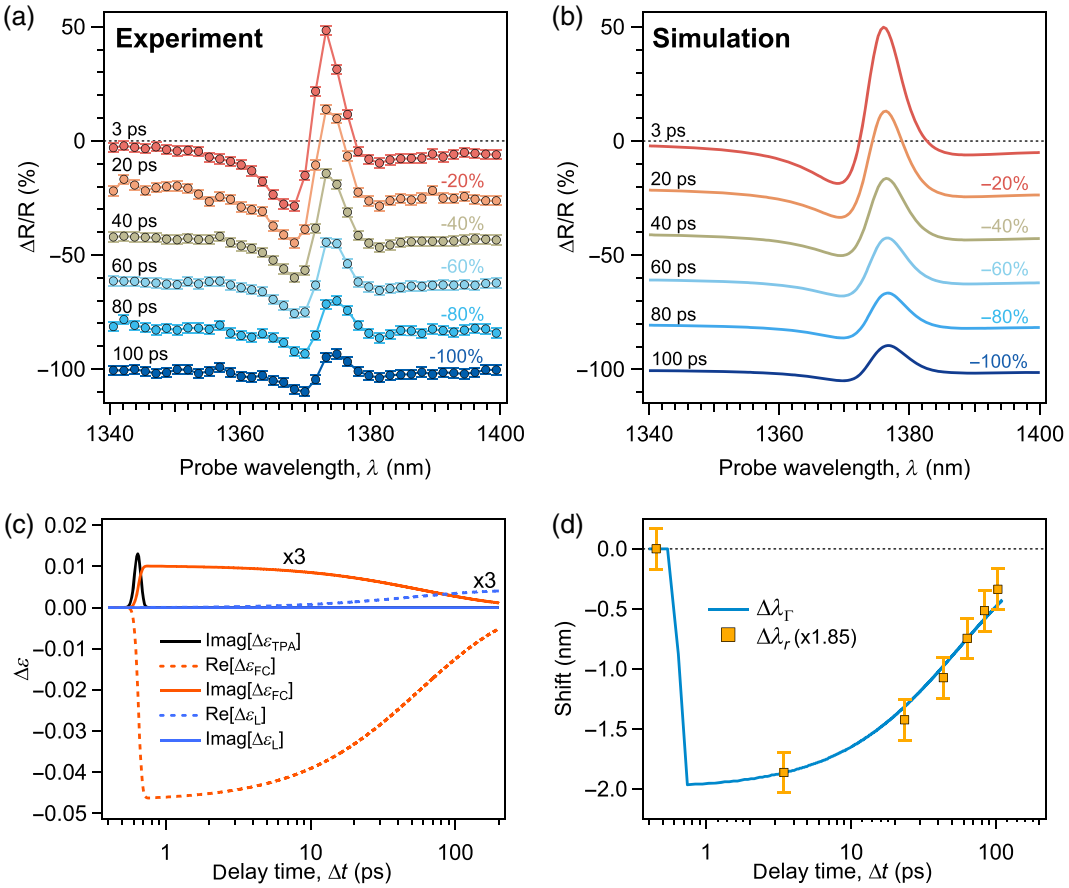

Fig. 2 (a) Experimental $\Delta R/R$ spectra at different time delays (denoted by the labels on the left side). For clarity, the curves are vertically shifted (labels on the right side). (b) Simulated $\Delta R/R$ spectra at the same time delays as in (a) employing CREM + RCWA model. For clarity, the curves are vertically shifted. (c) Real (Re, dashed line) and imaginary (Imag, solid line) parts of the individual components contributing to $\Delta\varepsilon$ calculated from the model analysis: TPA ($\Delta\varepsilon_{TPA}$), FC generation ($\Delta\varepsilon_{FC}$), and lattice heating ($\Delta\varepsilon_L$). The curves are horizontally shifted by 0.64 ps to visualize negative delay times on a logarithmic scale. (d) Temporal evolution of the shift: $\Delta\lambda_\Gamma$ from modal analysis (blue solid line) and $\Delta\lambda_r$ from differential fit (yelllow markers). The data (both solid line and markers) are horizontally shifted by 0.64 ps to visualize negative delay times on a logarithmic scale.

At this stage, it is useful to underline that the considered model, treating the FC density N, is not suitable for describing any coherence effect of the light–matter interaction under analysis. The chosen design of the theoretical model is based on the assumption that the temporal resolution of our setup (∼64 fs) is not capable of revealing the signature of coherence, since it is destroyed on a timescale of a few tens of femtoseconds in the case of solid-state platforms.[31,32,41–44]

Figure 2(b) shows the theoretical out-of-equilibrium spectra calculated via CREM + RCWA approach by assuming the parameters reported in Table 1. The theoretical model is capable of quantitatively reproducing the experimental out-of-equilibrium spectra in the whole temporal window under analysis by employing one fixed fitting parameter: the FC relaxation time τ_{rFC} (band edge carrier lifetime through single-carrier decay channels). Our analysis provides $\tau_{rFC} \sim 150$ ps, a value much shorter than that in bulk Si (>50 ns),[50] but comparable to that measured in other Si-based photonic structures.[51]

Table 1 Summary of the material parameter values adopted in this work for CREM + RCWA approach.

Parameter	Value	Units	Reference
C_p	1.66×10^6	J K^{-1} m^3	25
β_{TPA}	1.5×10^{-6}	m W^{-1}	25
ε_{Si}	$(5.3410 + i0.24127)^2$ at 410 nm	—	45
ε_{Si}, ε_{sub}	12.2 at 1370 nm	—	45
ε_{SiO_2}	2.09 at 1370 nm	—	46
η_1	1.888×10^{-4} at 1370 nm	K^{-1}	40
m_{eff}	$0.153 m_e$	—	47
τ_d	10	fs	48
γ	3×10^{-15}	m^3 s^{-1}	49

In order to better understand the role of FCs and lattice to the total $\Delta\varepsilon$, in Fig. 2(c), we show the temporal dynamics of $\Delta\varepsilon_{\mathrm{FC}}$, $\Delta\varepsilon_L$, and $\Delta\varepsilon_{\mathrm{TPA}}$ calculated by the CREM. As expected, the contribution due to TPA (black solid curve) is present only at very short time delays ($\Delta t < 1$ ps). The largest contribution to $\Delta\varepsilon$ in the probed time window is due to FC generation (red dashed and solid curves for real and imaginary parts, respectively), since the typical timescale is on the order of tens of picoseconds and lattice heating effects (blue solid and dashed curves for real and imaginary parts, respectively) manifest on longer timescales ($\Delta t > 100$ ps). $\Delta\varepsilon_L$ contribution is negligible in the probed time window due to the low (real-valued) thermo-optic coefficient.

The numerical results reported in Fig. 2(c) offer important insights into the physics of the NLM regarding the photoinduced dynamics of the GMR. Indeed, starting from the calculated $\Delta\varepsilon(\lambda, \Delta t)$, we can better describe this performing time-dependent modal analysis to retrieve the eigenvalue $\lambda_\Gamma^{\mathrm{out}}(\Delta t)$ of the GMR at each delay time. The retrieved time-dependent eigenvalue variation $\Delta\lambda_\Gamma(\Delta t) = \lambda_\Gamma^{\mathrm{out}}(\Delta t) - \lambda_\Gamma^{\mathrm{eq}}$, reported in Fig. 2(d) (blue solid line), suggests that the GMR experiences a blueshift after photoexcitation, reaching a maximum variation of the eigenwavelength $|\Delta\lambda_\Gamma^{\max}| \sim 2$ nm and then recovering to equilibrium on a timescale of 100 ps. Further, we adopt a differential fit procedure[26] based on a Fano line shape[52] to model the out-of-equilibrium spectra in Fig. 2(a). The experimental data can be reproduced assuming a resonance blueshift, which represents the FC-induced variation of the dielectric constant[31] (see Supplementary Material for more details). The retrieved blueshift temporal dynamics $\Delta\lambda_r(\Delta t)$, displayed in Fig. 2(d) (yellow markers), overlaps well with the $\Delta\lambda_\Gamma$ one.

Summarizing, the results in Fig. 2 highlight a nonnegligible difference regarding the order of magnitude between the optical response of the structure ($\Delta R/R \sim 50\%$ at maximum) and the modulation of the material properties ($\Delta\varepsilon/\varepsilon \sim 0.4\%$ and $\Delta\lambda/\lambda \sim 0.1\%$) following the moderate excitation of $180\,\mu\mathrm{J/cm^2}$. Therefore, in order to better investigate the role of the photonic structure in the interplay between the optical response and material properties variation, we report excitation-dependent pump–probe measurements on the NLM, and we compare the results to those obtained from a multilayer thin-film-like platform, consisting in a uniform Si (500 nm)/SiO_2 (1160 nm) bilayer[29] deposited on the Si substrate. [We underline that the thickness of the Si (SiO_2) layer in the thin-film-like sample is the same as d (h) in the NLM (see Appendix D).] In particular, we focus on the nonequilibrium FC-induced effect; therefore, we measure $\Delta R/R$ spectra of NLM at $\Delta t = 3$ ps, where the FC contribution dominates $\Delta\varepsilon$ [see Fig. 2(c)], for several excitation fluence (F_{inc}) levels in the 20 to 250-$\mu\mathrm{J/cm^2}$ range. We note that the maximum amplitude of the detected transient spectra, shown in Fig. 3(a), is 1 order of magnitude larger than that measured on the bilayer structure (see Table 2 and Fig. S5 in the Supplementary Material for more details), under similar excitation conditions and reflectance value in the at-equilibrium state. Therefore, the results clearly demonstrate the key role of the photonic structure (giving rise to spectral resonances exhibiting sharp edges), which allows one to enhance the transient modulation of the optical response [up to $\Delta R/R = 57\%$ at $\lambda = 1373$ nm; thus $\Delta R = 0.103$, in Fig. 3(a)] with respect to bulk-form material.

Moreover, the results in Fig. 3(a) reveal the key role of the GMR to achieve giant photoinduced reflectivity variations. From a general point of view, the amplitude of the $\Delta R/R$ spectra increases with increasing fluence (i.e., injected FC density); this is also accompanied by a blueshift of the spectra (i.e., the peak and valley of the transient spectra move toward lower wavelengths values as F_{inc} increases). The $\Delta\lambda_r(F_{\mathrm{inc}})$ trace, retrieved from the data by the differential-fit procedure, is shown in the inset of Fig. 3(a), and it is proportional to F_{inc} (black solid line). This behavior is due to the fact that, at the considered delay time (3 ps), $\Delta\varepsilon \simeq \Delta\varepsilon_{\mathrm{FC}} \propto N$. However, by carefully looking at the $\Delta R/R$ signal at 1367.5 nm [see Fig. 3(b)], we note that an initial linear regime (black dashed line) is followed by a saturation for fluences above 200 $\mu\mathrm{J/cm^2}$. The different behavior of the two quantities ($\Delta\lambda_r$ and $\Delta R/R$) can be interpreted on the basis of the Fano line shape of the GMR at equilibrium [Fig. 1(b)]. Indeed, the maximum achievable transient value is limited by the reflectance contrast (i.e., the difference between the minimum and maximum reflectance values) of the Fano resonance at equilibrium. Therefore, although the blueshift increases linearly with fluence (below the sample damage threshold), the transient

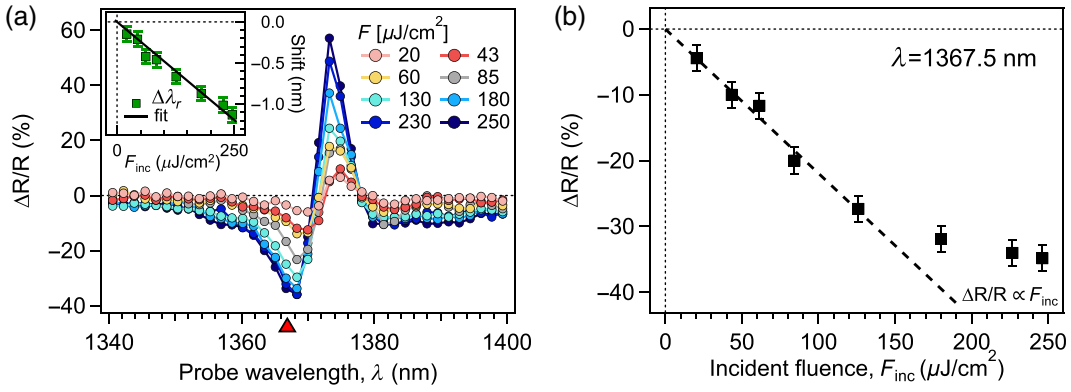

Fig. 3 (a) Experimental $\Delta R/R$ spectra measured for increasing fluence values. The inset reports the resonance shift $\Delta\lambda_r$ (retrieved from the measured $\Delta R/R$ spectra) as a function of the incident fluence, and the solid black line denotes a linear dependence. The red triangle denotes the probe wavelength value in which the data in (b) are taken. (b) Experimental minimum $\Delta R/R$ at $\lambda = 1367.5$ nm as a function of the fluence (black markers). The black dashed line denotes a linear dependence of the $\Delta R/R$ signal upon the fluence.

Table 2 Comparison between different metasurfaces[a].

Material	Platform	$\lvert\Delta R/R\rvert$ or $\lvert\Delta T/T\rvert$ (%)	Fluence	Reference
Si	Bulk single crystal (001)	7	16 mJ/cm^2	53
Si	Huygens	3	40 mJ/cm^2	54
Si	Bulk (001)	0.04	2.4 mJ/cm^2	32
Poly-Si	Nonlocal	57	250 μJ/cm^2	This work
Poly-Si	Nonlocal	27	130 μJ/cm^2	This work
Si, SiO_2	Bilayer	2.6	120 μJ/cm^2	This work
a-Si:H	Huygens	0.6	30 μJ/cm^2	23
a-Si:H	Huygens	8	800 μJ/cm^2	25
GaAs	Huygens	60	310 μJ/cm^2	24
GaAs-AlAs-InAs	QD embedded + Bragg mirror	20	2 to 3 mJ/cm^2	21
Au-ITO	Planar plasmonic crystal	80	NA	22
Au-Si	Grating	60	2 mJ/cm^2	55
V_2O_3	Thin film	14	8 mJ/cm^2	56

[a]QD, quantum dots; a-Si:H, hydrogenated amorphous silicon.

signal saturates. Overall, these results testify to the possibility of achieving large amplitude modulations also in the case of structure with moderate quality factor Q (in addition to those with high Q[51]). Thanks to the spectral properties of the GMR exhibited by the proposed Si-based NLM, the observed sizable modulation is achieved with intensity values much lower (up to 1 order of magnitude) than in other works, as summarized in Table 2. Performances in similar experimental conditions were reported[24] in the case of a GaAs-based metasurface. Despite being vastly employed for all-optical modulation due to efficient generation and recombination of FCs, GaAs does not exhibit such a widespread use in microelectronics and on-chip photonics as Si.[24]

3 Conclusions

In this work, we proposed an NLM to achieve giant modulation of the reflectivity on an ultrafast timescale. We provided evidence that such variation cannot be induced in bulk materials or thin films employing fluences below 250 μm/cm^2 and that the NLM plays a key role, i.e., it provided a sharp spectral variation, which ultimately leads to a giant reflectivity modulation mainly induced by FC generation. We described the experimental results employing a simple, yet effective, numerical approach based on CREM and RCWA simulations. We also unveiled the nonlinear dependence of the modulation depth as a function of the impinging fluence when the FCs are only responsible for the reflectivity variation. In addition to unveiling the physics of the ultrafast dynamics of photoexcited nonlocal Si metasurfaces, our results proved that it is possible to induce large modulation of the optical response inducing modest changes of the dielectric constant, which is of paramount importance in the design of ultrafast modulators and switches of the next generation, with reduced energy consumption and an ultrasmall footprint. Ultimately, the key ingredients for large optical modulation are the presence of a sharp variation in the linear response at equilibrium and its depth.

4 Appendix A: Fabrication

We oxidize using a wet process (H_2O-based) at 1100°C in a furnace (Tempress) a 500-μm-thick single-side polished $\langle 100\rangle$ Si wafer, yielding 1.1 μm thermal Si oxide. Then we coat the wafer with an amorphous silicon (a-Si) layer by means of low-pressure chemical vapor deposition. Silane (SiH_4) is used as a precursor. An additional dry oxidation and wet etching (vaporized HF) are performed to accurately determine the final thickness of the a-Si layer. The desired pattern is obtained using DUV lithography. The grating is suspended by performing a controlled and gentle etching of SiO_2. Further details about the fabrication process are provided elsewhere.[29,57]

5 Appendix B: Equilibrium Linear Spectroscopy

A home-built linear spectroscopy setup is employed to measure the (at equilibrium) reflectance of the NLM at normal incidence. We use a stabilized (fiber-coupled) tungsten–halogen lamp as a broadband light source (Thorlabs SLS201L). The white-light output is collimated by a parabolic mirror (Thorlabs RC12FC-P01). Before impinging on the sample, control over light polarization is accomplished by a polarizer (Thorlabs LPNIR100MP2) and a half-wave plate (Thorlabs AHWP10M-1600). The light passes through a beam splitter (Thorlabs BSN12R) and is focused on the sample by a lens (Thorlabs LA1251, NA = 0.02). The reflected light is collected by a parabolic mirror (Thorlabs RC12FC-P01), which is coupled to an optical fiber attached to a spectrometer (NIR-Quest 512-17).

6 Appendix C: Numerical Simulations

The temporal dynamics of carrier density $[N(\Delta t)]$, lattice temperature $[T(\Delta t)]$, and intensity $[I(\Delta t)]$are described by the following CREM consisting of a system of two coupled-ordinary differential equations,

$$\begin{cases} \dot{N}(\Delta t) = -[\gamma N(\Delta t) + \tau_{\mathrm{rFC}}^{-1}]N(\Delta t) + \Psi(\Delta t), \\ C_p \cdot \dot{T}(\Delta t) = E_{\mathrm{eh}}[\gamma N(\Delta t) + \tau_{\mathrm{rFC}}^{-1}]N(\Delta t), \end{cases} \tag{4}$$

where γ is the bimolecular recombination rate, τ_{rFC} is the FC relaxation time, C_p is the Si volumetric specific heat, E_{eh} is the electron–hole pair energy, and $\Psi(\Delta t)$ is the time-dependent FC generation rate per unit volume. Given the model accounting for linear and nonlinear carrier absorption, E_{eh} is equal to $2\pi\hbar c/\lambda_p$ for single-photon absorption or $4\pi\hbar c/\lambda_p$ for TPA. Moreover, $\Psi(\Delta t) = \Phi(\Delta t) + \Phi_{\mathrm{TPA}}(\Delta t)$, where the linear and nonlinear contributions are calculated as $\Phi(\Delta t) = A\lambda_p I(\Delta t)/(2\pi\hbar c d)$ and $\Phi_{\mathrm{TPA}}(\Delta t) = A_{\mathrm{TPA}}(I)\lambda_p I(\Delta t)/(4\pi\hbar c d)$, respectively, with A [$A_{\mathrm{TPA}} = 1 - e^{-\beta_{\mathrm{TPA}} \cdot I(\Delta t) \cdot d}$] being the linear (nonlinear) absorption and d being the top Si layer thickness. We numerically solve the system in Eq. (4) assuming a Gaussian temporal profile for the intensity of the pump laser pulse $I(\Delta t) = \sqrt{2/\pi} \cdot (F_{\mathrm{inc}}/\tau_p) \cdot \exp(-2\Delta t^2/\tau_p^2)$, with $\tau_p = 64$ fs.

The equilibrium reflectance ($R_{\mathrm{RCWA}}^{\mathrm{eq}}$) of the NLM is calculated[29] via RCWA[58,59] as the zeroth order back-diffraction efficiency ($\mathrm{DE}_{r,0}$), by assuming geometrical parameters obtained from SEM analysis of the fabricated NLM and dispersionless permittivities of the Si grating ($\varepsilon_{\mathrm{Si}}$), SiO_2 buffer layer ($\varepsilon_{\mathrm{SiO_2}}$), and Si substrate ($\varepsilon_{\mathrm{sub}}$). In particular, starting from Refs. 45 and 46, the optical properties values are optimized (deviations <1%) to improve the matching between the calculated $R_{\mathrm{RCWA}}^{\mathrm{eq}}$ and the experimental data [Fig. 1(b)]. The out-of-equilibrium reflectance spectrum is calculated via RCWA as $R_{\mathrm{RCWA}}^{\mathrm{out}} = DE_{r,0}(\varepsilon_{\mathrm{Si}} + \Delta\varepsilon, \varepsilon_{\mathrm{SiO2}}, \varepsilon_{\mathrm{sub}})$, where the Si permittivity $\varepsilon_{\mathrm{Si}}$ is modified by the variation $\Delta\varepsilon$ according to Eqs. (1)–(3), thus assuming only a photoinduced variation of the grating optical properties.

7 Appendix D: Time-Resolved Spectroscopy

Time-resolved spectroscopy measurements are performed in a home-built pump–probe setup. The system is based on a femtosecond laser (Monaco, Coherent) delivering 300 fs pulses centered at 1035 nm wavelength with 40 μJ energy at a 1 MHz repetition rate. The laser output feeds a hybrid optical parametric amplifier (Opera-F, Coherent) generating idler (IDL) and signal (SIG) beams. The IDL central wavelength is tuned at ~1400 nm (bandwidth 100 nm, full width at half-maximum) and represents the probe beam of the experiment. The SIG output radiation, centered at 820 nm, is frequency-doubled in a 6-mm thick barium borate crystal to generate second-harmonic radiation at $\lambda_p = 410$ nm (with a maximum pulse energy of 60 nJ); the latter is employed as the pump beam in the experiments. The residual component of the 820 nm signal is removed from the pump radiation by a bandpass filter (Thorlabs FESH0700). The intensity of the pump radiation impinging onto the sample is controlled by a variable neutral density filter (Thorlabs NDC-100C-4). In order to control the delay between the pump and probe arrival time (at sample position), the optical path length of the former is varied by a motorized linear delay stage (Newport M-ILS150CCL). The pump and probe beams are linearly orthogonally polarized, with the former being horizontal and the latter vertical. In order to ensure a proper collection of the reflected radiation, the probe beam impinges onto the sample at slightly off-normal incidence ($\varphi \sim 4$ deg). After the interaction with the sample, the reflected probe beam is collected and then dispersed on a spectrometer to achieve moderate spectral resolution (1.5 nm in the 1300 to 1500 nm spectral region). In particular, the reflected probe spectrum is measured when the pump does (not) reach the sample, R^{on} (R^{off}), and this provides the out-of-equilibrium (at-equilibrium) reflectance R_{out} (R_{eq}). The relative reflectance variation spectrum is then calculated as $\Delta R/R = (R_{\mathrm{out}} - R_{\mathrm{eq}})/R_{\mathrm{eq}} = (R^{\mathrm{on}} - R^{\mathrm{off}})/R^{\mathrm{off}}$ (see Supplementary Material for more details).

Disclosures

The authors declare no conflicts of interests.

Code and Data Availability

All data in support of the findings of this paper are available within the article or as Supplementary Material.

Acknowledgments

C. De Angelis and O. Sergaeva would like to acknowledge the support of the Russian Science Foundation (Grant No. 22-12-00204). C. De Angelis also would like to acknowledge the financial support from the European Community through the "METAFAST" Project (H2020-FETOPEN-2018-2020, Grant No. 899673) and the Ministero Italiano dell'Istruzione (MIUR) through the "METEOR" Project (No. PRIN-2020, 2020EYLJT_002). A. Tognazzi thanks the European Union for the financial support through "FESR o FSE, PON Ricerca e Innovazione 2014-2020-DM 1062/2021" and the University of Palermo through "Fondo Finalizzato alla Ricerca di Ateneo 2023." A. C. Cino acknowledges financial support from the European Union, NextgenerationEU, MUR D.M 737/2021, through the Project "Eurostart22" (No. PRJ-0988).

References

1. D. R. Smith, J. B. Pendry, and M. C. K. Wiltshire, "Metamaterials and negative refractive index," *Science* **305**, 788–792 (2004).
2. K. Shastri and F. Monticone, "Nonlocal flat optics," *Nat. Photonics* **17**, 36–47 (2022).
3. M. Khorasaninejad et al., "Metalenses at visible wavelengths: diffraction-limited focusing and subwavelength resolution imaging," *Science* **352**, 1190–1194 (2016).
4. G.-H. Go et al., "Scannable dual-focus metalens with hybrid phase," *Nano Lett.* **23**, 3152–3158 (2023).
5. Y. Hu et al., "All-dielectric metasurfaces for polarization manipulation: principles and emerging applications," *Nanophotonics* **9**, 3755–3780 (2020).
6. K. I. Okhlopkov et al., "Tailoring third-harmonic diffraction efficiency by hybrid modes in high-Q metasurfaces," *Nano Lett.* **21**, 10438–10445 (2021).
7. S. M. Kamali et al., "A review of dielectric optical metasurfaces for wavefront control," *Nanophotonics* **7**, 1041–1068 (2018).
8. M. Rahmani et al., "Reversible thermal tuning of all-dielectric metasurfaces," *Adv. Funct. Mater.* **27**, 1700580 (2017).
9. Z. Guanxing et al., "Reconfigurable metasurfaces with mechanical actuations: towards flexible and tunable photonic devices," *J. Opt.* **23**, 013001 (2020).
10. K. Nishida et al., "All-optical scattering control in an all-dielectric quasi-perfect absorbing Huygens' metasurface," *Nanophotonics* **12**, 139–146 (2022).
11. A. Afridi et al., "Ultrathin tunable optomechanical metalens," *Nano Lett.* **23**, 2496–2501 (2023).

12. Y. Hu et al., "Electrically tunable multifunctional polarization-dependent metasurfaces integrated with liquid crystals in the visible region," *Nano Lett.* **21**, 4554–4562 (2021).
13. Z. Yang et al., "Phase-only tuning of extreme Huygens metasurfaces enabled by optical anisotropy," *Adv. Opt. Mater.* **10**, 2101893 (2021).
14. J. Shabanpour, S. Beyraghi, and A. Cheldavi, "Ultrafast reprogrammable multifunctional vanadium-dioxide-assisted metasurface for dynamic THz wavefront engineering," *Sci. Rep.* **10**, 8950 (2020).
15. A. Tripathi et al., "Tunable mie-resonant dielectric metasurfaces based on VO_2 phase-transition materials," *ACS Photonics* **8**, 1206–1213 (2021).
16. A. Tognazzi et al., "Opto-thermal dynamics of thin-film optical limiters based on the VO_2 phase transition," *Opt. Mater. Express* **13**, 41–52 (2022).
17. B. Li et al., "Fundamental limits for transmission modulation in VO_2 metasurfaces," *Photonics Res.* **11**, B40–B49 (2022).
18. D. de Ceglia et al., "Transient guided-mode resonance metasurfaces with phase-transition materials," *Opt. Lett.* **48**, 2961–2964 (2023).
19. Y. Che et al., "Tunable optical metasurfaces enabled by multiple modulation mechanisms," *Nanophotonics* **9**, 4407–4431 (2020).
20. L. Carletti et al., "Reconfigurable nonlinear response of dielectric and semiconductor metasurfaces," *Nanophotonics* **10**, 4209–4221 (2021).
21. P. P. Iyer et al., "Sub-picosecond steering of ultrafast incoherent emission from semiconductor metasurfaces," *Nat. Photonics* **17**, 588–593 (2023).
22. M. Taghinejad et al., "Ultrafast control of phase and polarization of light expedited by hot-electron transfer," *Nano Lett.* **18**, 5544–5551 (2018).
23. M. R. Shcherbakov et al., "Ultrafast all-optical switching with magnetic resonances in nonlinear dielectric nanostructures," *Nano Lett.* **15**, 6985–6990 (2015).
24. M. R. Shcherbakov et al., "Ultrafast all-optical tuning of direct-gap semiconductor metasurfaces," *Nat. Commun.* **8**, 17 (2017).
25. G. Della Valle et al., "Nonlinear anisotropic dielectric metasurfaces for ultrafast nanophotonics," *ACS Photonics* **4**, 2129–2136 (2017).
26. P. Franceschini et al., "Tuning the ultrafast response of Fano resonances in halide perovskite nanoparticles," *ACS Nano* **14**, 13602–13610 (2020).
27. C. Giannetti et al., "Thermomechanical behavior of surface acoustic waves in ordered arrays of nanodisks studied by near-infrared pump–probe diffraction experiments," *Phys. Rev. B* **76**, 125413 (2007).
28. Z. Chai et al., "Ultrafast all-optical switching," *Adv. Opt. Mater.* **5**, 1600665 (2016).
29. P. Franceschini et al., "Nonlocal resonances in pedestal high-index-contrast metasurfaces based on a silicon-on-insulator platform," *Appl. Phys. Lett.* **123**, 071701 (2023).
30. M. F. Limonov et al., "Fano resonances in photonics," *Nat. Photonics* **11**, 543–554 (2017).
31. A. Othonos, "Probing ultrafast carrier and phonon dynamics in semiconductors," *J. Appl. Phys.* **83**, 1789–1830 (1998).
32. A. J. Sabbah and D. M. Riffe, "Femtosecond pump–probe reflectivity study of silicon carrier dynamics," *Phys. Rev. B* **66**, 165217 (2002).
33. J. R. Goldman and J. A. Prybyla, "Ultrafast dynamics of laser-excited electron distributions in silicon," *Phys. Rev. Lett.* **72**, 1364–1367 (1994).
34. S. Jeong and J. Bokor, "Ultrafast carrier dynamics near the Si(100) 2×1 surface," *Phys. Rev. B* **59**, 4943–4951 (1999).
35. F. Gambino et al., "A review on dielectric resonant gratings: mitigation of finite size and Gaussian beam size effects," *Results Opt.* **6**, 100210 (2022).
36. A. Di Cicco et al., "Broadband optical ultrafast reflectivity of Si, Ge and GaAs," *Sci. Rep.* **10**, 17363 (2020).
37. B. Bennett, R. Soref, and J. Del Alamo, "Carrier-induced change in refractive index of InP, GaAs and InGaAsP," *IEEE J. Quantum Electron.* **26**, 113–122 (1990).
38. K. Sokolowski-Tinten and D. von der Linde, "Generation of dense electron-hole plasmas in silicon," *Phys. Rev. B* **61**, 2643–2650 (2000).
39. A. Esser et al., "Ultrafast recombination and trapping in amorphous silicon," *Phys. Rev. B* **41**, 2879–2884 (1990).
40. G. Ghosh, *Handbook of Optical Constants of Solids: Handbook of Thermo-Optic Coefficients of Optical Materials with Applications*, Academic Press (1998).
41. R. Tomasiunas et al., "Femtosecond dephasing in porous silicon," *Appl. Phys. Lett.* **68**, 3296–3298 (1996).
42. H. Petek and S. Ogawa, "Femtosecond time-resolved two-photon photoemission studies of electron dynamics in metals," *Prog. Surf. Sci.* **56**, 239–310 (1997).
43. W. Nessler et al., "Femtosecond time-resolved study of the energy and temperature dependence of hot-electron lifetimes in $Bi_2CaCu_2O_8$," *Phys. Rev. Lett.* **81**, 4480–4483 (1998).
44. P. Franceschini et al., "Coherent control of the orbital occupation driving the insulator-to-metal Mott transition in V_2O_3," *Phys. Rev. B* **107**, L161110 (2023).
45. C. Schinke et al., "Uncertainty analysis for the coefficient of band-to-band absorption of crystalline silicon," *AIP Adv.* **5**, 067168 (2015).
46. I. H. Malitson, "Interspecimen comparison of the refractive index of fused silica," *J. Opt. Soc. Am.* **55**, 1205–1209 (1965).
47. H. M. van Driel, "Kinetics of high-density plasmas generated in Si by 1.06- and 0.53-μm picosecond laser pulses," *Phys. Rev. B* **35**, 8166–8176 (1987).
48. B. E. Sernelius, "Intraband relaxation time in highly excited semiconductors," *Phys. Rev. B* **43**, 7136–7144 (1991).
49. K. E. Myers, Q. Wang, and S. L. Dexheimer, "Ultrafast carrier dynamics in nanocrystalline silicon," *Phys. Rev. B* **64**, 161309 (2001).
50. C.-M. Li, T. Sjodin, and H.-L. Dai, "Photoexcited carrier diffusion near a Si(111) surface: non-negligible consequence of carrier-carrier scattering," *Phys. Rev. B* **56**, 15252–15255 (1997).
51. V. R. Almeida et al., "All-optical control of light on a silicon chip," *Nature* **431**, 1081–1084 (2004).
52. U. Fano, "Effects of configuration interaction on intensities and phase shifts," *Phys. Rev.* **124**, 1866–1878 (1961).
53. A. Di Cicco et al., "Broadband optical ultrafast reflectivity of Si, Ge and GaAs," *Sci. Rep.* **10**, 17363 (2020).
54. D. G. Baranov et al., "Nonlinear transient dynamics of photoexcited resonant silicon nanostructures," *ACS Photonics* **3**, 1546–1551 (2016).
55. J. N. Caspers, N. Rotenberg, and H. M. van Driel, "Ultrafast silicon-based active plasmonics at telecom wavelengths," *Opt. Express* **18**, 19761–19769 (2010).
56. A. Ronchi et al., "Nanoscale self-organization and metastable non-thermal metallicity in mott insulators," *Nat. Commun.* **13**, 3730 (2022).
57. L. Y. Beliaev et al., "Pedestal high-contrast gratings for biosensing," *Nanomaterials* **12**, 1748 (2022).
58. M. G. Moharam et al., "Formulation for stable and efficient implementation of the rigorous coupled-wave analysis of binary gratings," *J. Opt. Soc. Am. A* **12**, 1068–1076 (1995).
59. L. Li, "Formulation and comparison of two recursive matrix algorithms for modeling layered diffraction gratings," *J. Opt. Soc. Am. A* **13**, 1024–1035 (1996).

Andrea Tognazzi is a researcher at the University of Palermo, Italy. He received his bachelor's and MSc degrees from the Catholic University of Sacred Heart in Brescia, Italy, and his PhD from the University of Brescia. His research interests are in the fields of nonlinear optics, reconfigurable metasurfaces, and nanophotonics.

Paolo Franceschini is a postdoctoral researcher at the Department of Information Engineering of University of Brescia (Italy). He received his PhD (dual degree) in 2022 from Catholic University of the Sacred Heart (Italy) and Katholieke Universiteit Leuven (Belgium) with a joint research project within the International Doctoral Program in Science. Research interests focus on nonlinear optics, time-resolved spectroscopy, and photonics.

Olga Sergaeva is a researcher at the Department of Information Engineering of the University of Brescia (Italy). She received her BS, MS, and PhD (2013) at ITMO University (St. Petersburg, Russia), and had a postdoctoral fellowship (2016-2018) at the University of Missouri (Columbia, Missouri, USA). Her research interests include ultrafast light–matter interaction, nonlinear optics, nanophotonics, and reconfigurable metasurfaces.

Giovanni Finco received two MSc degrees, in telecommunication engineering from the University of Padova (Italy) and in photonics engineering from the Technical University of Denmark under the Top International Managers for Engineering Programme. He is currently employed as a doctoral researcher in the Physics Department of the Federal Institute of Technology in Zurich, Switzerland, where he develops lithium-niobate-on-insulator photonic integrated circuits technology for classical and quantum applications.

Andrei V. Lavrinenko received the PhD and DSci degrees from the Belarusian State University, Minsk, Belarus, in 1989 and 2004, respectively. Since 2004, he has been an associate professor with the Department of Electrical and Photonic Engineering at Technical University of Denmark. Since 2008, he has been leading the Metamaterials Group of this department. He is the author of more than 220 journal papers. His research interests include metamaterials, plasmonics, photonic crystals, and numerical methods.

Alfonso C. Cino received his PhD in electronic engineering from the University of Palermo, Italy, in 1998. He was the head of the Optical Technologies Lab at CRES (Center for Electronic Research in Sicily) until 2010. Currently he is an associate professor of electromagnetic fields at the University of Palermo. His research interests have been thin films, integrated optics, nonlinear frequency conversion, optical sensors, terahertz sources, photovoltaics, quantum optics, and optical metasurfaces.

Domenico de Ceglia is associate professor of electromagnetic fields and optics at University of Brescia, Italy. He received his PhD in electronic engineering from Politecnico di Bari, Italy, in 2007. He has been a senior research associate at the US Army C. Bowden Research Center. His research is focused on electromagnetics, optics, and photonics, with emphasis on light–matter interactions in nanostructures. He is a member of IEEE and a senior member of Optica.

Biographies for the other authors are not available.